

Microscale Modeling of Creep Deformation and Rupture in Nickel-based Superalloy IN 617 at High Temperature

Van-Tung Phan, Xiang Zhang, Yumeng Li and Caglar Oskay*

*Department of Civil and Environmental Engineering
Vanderbilt University
Nashville, TN 37235*

Abstract

This manuscript presents the computational modeling and analysis of creep deformation and failure of Nickel-based superalloy, Inconel 617 (IN 617), operating at high temperature. Crystal plasticity finite element (CPFE) approach, considering isothermal and large deformation conditions at the microstructural scale has been extended for creep deformation and rupture modeling of IN 617 at 950°C. In order to accurately capture the creep strains that accumulate particularly at relatively low stress levels, a dislocation climb model has been incorporated into the CPFE framework. In addition, a cohesive zone (CZ) model is adopted to capture intergranular creep damage, and incorporated into the CPFE framework. The CPFE and the CZ models work in tandem to describe the viscoplastic deformation as well as progressive failure in the material microstructure. The calibration of dislocation climb and CZ parameters is performed based on experimental data. The microstructure model is validated using independent creep experiments performed at various stress levels. Microstructural analysis of the stress and damage distributions as well as their time-dependent evolution is carried out to provide insight into the dominant microscale deformation and failure mechanisms. Creep life predictions are performed to describe rupture life as a function of load amplitude at high temperature.

Keywords: crystal plasticity modeling, Nickel-based superalloy, dislocation climb, cohesive zone model, inter-granular damage, creep

1 Introduction

Very high temperature reactor (VHTR) is a promising concept in Generation IV nuclear systems for its highly efficient electricity generation and hydrogen production. VHTR environ-

*Corresponding author address: VU Station B#351831, 2301 Vanderbilt Place, Nashville, TN 37235. Email: caglar.oskay@vanderbilt.edu

ments pose significant challenges to structural materials due to the presence of extremely high temperatures (up to 950°C) combined with mechanical loading for long periods of time [1]. The main objective of this work is to establish a microstructure model that accurately describes the creep deformation and consequent rupture of IN 617 at high temperature, which is a candidate structural material for such extreme environment applications.

Experimental studies by Benz et al. [5], Kim et al. [24, 26], Lillo and Wright [31], Lillo et al. [32], Martino et al. [34], Roy et al. [44], and Wright et al. [56] recently investigated the behavior of IN 617 subjected to creep loads at high temperatures under various levels of applied stresses. Experimental observations of microstructures using optical microscopy show significant atomic mobility and creep deformation even at relatively low stresses. As observed in experimental creep curves [4, 5, 24, 25, 44], a relatively short primary and secondary creep regime is followed by a long tertiary creep regime. In particular, a well-defined secondary creep was not observed. A rapid rise in creep rate caused by an increase in mobile dislocation density can reduce or exclude the secondary creep stage. This is known as sigmoidal creep behavior, and has been observed in Nickel-based alloys [53].

A primary mechanism for creep strains is dislocation climb resulting in a power law creep behavior of metals at high temperatures [36]. Prior experimental observations performed on creep deformation of IN 617 indicate that the minimum creep exponent typically lies between 5-7 within the 850-950°C temperature range [5, 26, 45]. This range indicates the presence of combined dislocation glide and climb [21], typically observed for class II alloys.

Crystal plasticity finite element (CPFE) method has been a well-established approach that can accurately capture deformation and failure mechanisms at the microscale (see, e.g., Roters et al. [42]). The CPFE framework has been previously employed to characterize creep deformation in Nickel-based alloys [23] as well as other materials (e.g., [46]). More recently, Zhang and Oskay [61] employed CPFE to describe deformation in IN 617 microstructures subjected fatigue and creep-fatigue cycles. This study incorporated a solute drag creep model to describe short term time-dependent behavior. The current manuscript builds on this model to describe high temperature creep in IN 617.

Dislocation climb that results from the interactions between dislocations and local non-equilibrium concentrations of point defects at high temperature contributes significantly to the irreversible deformation under creep loads [29, 30]. Therefore, it is necessary to include dislocation climb mechanism into a microstructure model to capture the viscoplastic deformation under high temperature loading conditions. Lebensohn et al. [29] extended their visco-plastic self-consistent (VPSC) formulation to consider coupled glide-climb mechanism and arrived at improved predictions of the behavior of olivine polycrystalline aggregates. Geers et al. [13] proposed an extended strain gradient crystal plasticity model by incorporating the effects of dislocation climb into the plastic strain evolution in the context of strain gradient plasticity. The coupled glide-climb theory was verified through analysis of dislocation interactions in either bypassing of an elastic precipitate or destruction of dislocation pile-ups at the mesoscale. Huang et al. [19] investigated the influence of dislocation climb on the grain size dependent

response and its underlying mechanisms. Other investigations (e.g., [16, 57]) employed discrete dislocation dynamics framework to study single crystal Ni-based superalloys. Vacancy diffusion-induced dislocation climb was found to be critical to describe the strain rate effect on the early plastic behavior of high-temperature and low-stress creep of Ni-based superalloys.

Post-mortem microstructural examinations by Kim et al. [24, 25] revealed that the creep damage and fracture in IN 617 is predominantly intergranular. Creep damage and ultimate rupture have been linked to the formation, growth and coalescence of grain boundary cavities, in addition to oxidation and other mechanisms. The recent experimental study by Tahir et al. [54] also confirms that damage caused by creep is of intergranular in nature.

While the incorporation of the dislocation climb allows modeling of the creep deformations accurately up to the onset of significant intergranular damage, it does not account for the progressive creep damage accumulation at grain boundaries. Cohesive zone modeling (CZM) originally proposed by Barenblatt [3] and Dugdale [12] is an effective approach to model progressive failure (e.g., [18, 20]), particularly in the presence of pre-defined paths of failure (e.g., intergranular fracture). In order to model the intergranular cracking at the microscale, cohesive elements with zero thickness are directly embedded between the adjacent grains to explore normal (i.e., mode I) and normal-and-shear (i.e., mixed mode) damage initiation. The present manuscript employs the CZM approach along with CPFE that includes glide-climb mechanisms in predicting the deformation as well as progressive damage accumulation in IN 617 subjected to creep loads.

Some recent numerical investigations employed combined CPFE-CZM approach to model damage behavior at individual grain boundaries in plastically deforming metals [11, 48, 49, 27]. Simonovski and Cizelj [48, 49] demonstrated the initiation and evolution states of the intergranular cracking using cohesive zone in 3D polycrystalline aggregates for AISI 304 stainless steel. In the work of Kupka and coworkers [27] for an Aluminum-Lithium alloy, a fracture analysis is performed using cohesive zone modeling of the grain boundary, which allows for a mechanism independent description of the fracture process. Gonzalez et al. [14] adopted a CPFE model that embedded isotropic cohesive elements at grain boundaries to examine the effect of elevated grain boundary stresses on fracture behavior. While creep fracture phenomenon observed in experiments [2, 22] were numerically modeled by Onck and van der Giessen [37, 38] for a polycrystalline material at the microscale, a combination of CPFE and CZM has not been used, to the best of the authors' knowledge, in capturing creep deformation and simulating the formation and growth of cavities in polycrystalline aggregates.

In this manuscript, a computational microstructure model is developed to capture creep deformation and failure behavior in IN 617 operating at high temperature. This model is based on an isothermal, large deformation CPFE formulation and idealizes the deformation in the crystal lattice as collective glide and climb of dislocations. In particular, the proposed work is built on a glide-based CPFE framework previously developed by the authors [61] and incorporates a dislocation climb model originally proposed by Lebensohn and coworkers [29, 30] for capturing the viscoplastic deformation within the grains while grain boundary damage is

modeled by CZM. The CPFE and the CZ models work in tandem to compute the viscoplastic deformation as well as progressive failure in the material microstructure. Model parameters are calibrated and validated using experimental creep tests at different hold stress amplitudes. Microscale stress and damage distribution as well as their evolution during the creep process are analyzed to gain further understanding of the underlying deformation mechanisms.

The remainder of this manuscript is organized as follows: Section 2 introduces the combined CPFE-CZM framework, which starts by an overview of the glide-based CPFE model and its extension to account for dislocation climb, followed by the incorporation of cohesive zone model, where creep damage evolution equations and numerical implementation are discussed in detail. The microstructure model preparation and incorporation of cohesive elements are discussed in Section 3. Section 4 describes the calibration process of the model for IN 617. In Section 5, microstructural analysis and validation of the model are presented. Finally, Section 6 summarizes this manuscript and discusses the future work.

2 Constitutive Models

Using the virtual work principle, the sum of the strain energy in the domain and the cohesive fracture energy on the intergranular fracture surfaces are equal to the virtual work done by external traction along the boundary (ignoring body forces). The weak form of governing equilibrium equation is expressed as:

$$\int_{\Omega} \mathbf{S} : \delta \mathbf{E} d\Omega + \int_{\Gamma_{\text{GB}}} \mathbf{T} : \delta [[\mathbf{u}]] d\Gamma = \int_{\Gamma_t} \hat{\mathbf{T}} \cdot \delta \mathbf{u} d\Gamma \quad (1)$$

in which, \mathbf{S} is the second Piola Kirchhoff stress, \mathbf{T} the tractions along the grain boundaries idealized as sharp interfaces and denoted as Γ_{GB} , and $\hat{\mathbf{T}}$ the prescribed tractions along the Neumann boundaries of the representative volume domain. $\delta \mathbf{u}$, $\delta \mathbf{E}$ and $\delta [[\mathbf{u}]]$ denote the variations of the displacement, Green-Lagrange strain, and grain boundary displacement jump fields, respectively. In the present formulation, the weak form is closed by the stress-strain relationship within the grains and the traction-displacement jump relationship (i.e., cohesive law) across the grain boundaries.

2.1 Crystal plasticity model with dislocation glide and climb

Crystal plasticity finite element method is a powerful and versatile tool that has been adopted to solve crystal plasticity problems under various loading conditions to understand microstructural deformation mechanisms (for a comprehensive review, see Ref. [43]). The deformation gradient \mathbf{F} is multiplicatively decomposed into elastic stretch (\mathbf{V}^e), elastic rotation (\mathbf{R}^e) and plastic (\mathbf{F}^p) contributions [33]:

$$\mathbf{F} = \mathbf{V}^e \cdot \mathbf{R}^e \cdot \mathbf{F}^p \quad (2)$$

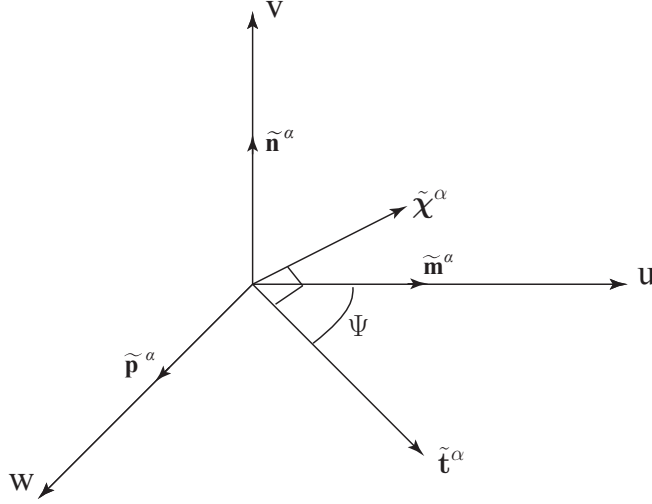


Figure 1: Illustration of dislocation orientation: coordinate system $u - v - w$ is aligned with dislocation glide system α ($\tilde{\mathbf{p}}^\alpha$ is the unit vector to complete a right-hand orthogonal coordinate system defined by $\tilde{\mathbf{n}}^\alpha$ and $\tilde{\mathbf{m}}^\alpha$) and dislocation climb orientation depends the angle ψ formed by the dislocation line $\tilde{\mathbf{t}}^\alpha$ and the slip direction $\tilde{\mathbf{m}}^\alpha$.

which introduces two intermediate configurations, $\tilde{\mathbb{B}}$ and $\tilde{\mathbb{B}}$ between the initial and current configurations, \mathbb{B}_0 and \mathbb{B} . Configuration $\tilde{\mathbb{B}}$ is chosen to express the crystal constitutive equations, which is obtained by elastically unloading the current configuration through \mathbf{V}^{e-1} . The velocity gradient in configuration $\tilde{\mathbb{B}}$ is decomposed into symmetric ($\tilde{\mathbf{D}}^p$) and skew ($\tilde{\mathbf{W}}^p$) parts as:

$$\tilde{\mathbf{L}}^p = \tilde{\mathbf{D}}^p + \tilde{\mathbf{W}}^p \quad (3)$$

both of which have contributions from dislocation glide (indicated by subscript g) and climb (indicated by subscript c):

$$\begin{aligned} \tilde{\mathbf{D}}^p &= \tilde{\mathbf{D}}_g^p + \tilde{\mathbf{D}}_c^p \\ \tilde{\mathbf{W}}^p &= \tilde{\mathbf{W}}_g^p + \tilde{\mathbf{W}}_c^p \end{aligned} \quad (4)$$

A dislocation glide based model for IN 617 at high temperature has been previously developed, calibrated and verified (for details, see [61]). The dislocation model as well as the calibrated parameters are kept the same in this work and skipped for brevity. While the dislocation-glide-based model can accurately capture the response of the polycrystal subjected to a fatigue or a creep-fatigue cycle, the ability to capture the long-term creep deformation, particularly at stress levels much lower than the yield stress, requires the inclusion of the dislocation climb mechanism. The rate of deformation and spin contributions of dislocation climb

are expressed as [29]:

$$\begin{aligned}\tilde{\mathbf{D}}_c^p &= \mathbf{R}^e \cdot \sum_{\alpha=1}^N \dot{\gamma}_c^\alpha (\mathbf{m}_0^\alpha \otimes \boldsymbol{\chi}_0^\alpha)_S \cdot \mathbf{R}^{eT} = \sum_{\alpha=1}^N \dot{\gamma}_c^\alpha (\tilde{\mathbf{K}}^\alpha)_S \\ \tilde{\mathbf{W}}_c^p &= \mathbf{R}^e \cdot \sum_{\alpha=1}^N \dot{\gamma}_c^\alpha (\mathbf{m}_0^\alpha \otimes \boldsymbol{\chi}_0^\alpha)_A \cdot \mathbf{R}^{eT} = \sum_{\alpha=1}^N \dot{\gamma}_c^\alpha (\tilde{\mathbf{K}}^\alpha)_A\end{aligned}\quad (5)$$

in which, $\dot{\gamma}_c^\alpha$ is the shear strain rate as a result of dislocation climb. $\tilde{\mathbf{K}}^\alpha = \tilde{\mathbf{m}}^\alpha \otimes \tilde{\boldsymbol{\chi}}^\alpha$ is the climb tensor associated with the slip system α in the crystal coordinate system [17, 29], and $\tilde{\boldsymbol{\chi}}^\alpha$ the unit vector parallel to the product of normal to the glide plane ($\tilde{\mathbf{n}}^\alpha$) and the tangent to the dislocation line ($\tilde{\mathbf{t}}^\alpha$) defined as:

$$\tilde{\boldsymbol{\chi}}^\alpha = \tilde{\mathbf{n}}^\alpha \times \tilde{\mathbf{t}}^\alpha \quad (6)$$

It is straightforward to see that the climb tensor depends on the dislocation orientation with respect to the glide coordinate system, and this dependence is expressed in terms of a single parameter ψ (i.e., the angle between $\tilde{\mathbf{t}}^\alpha$ and $\tilde{\mathbf{m}}^\alpha$) as shown in Fig. 1. The climb tensor is then expressed as:

$$\tilde{\mathbf{K}}^\alpha = [\tilde{\mathbf{m}}^\alpha \otimes (\tilde{\mathbf{m}}^\alpha \times \tilde{\mathbf{n}}^\alpha)] \cos\psi + (\tilde{\mathbf{m}}^\alpha \otimes \tilde{\mathbf{m}}^\alpha) \sin\psi \quad (7)$$

which resolves the applied shear stress into an individual climb system as $\tau_c^\alpha = \boldsymbol{\tau} : (\tilde{\mathbf{K}}^\alpha)_{\text{dev}}$ and accumulates the climb strain based on a climb flow rule given by:

$$\dot{\gamma}_c^\alpha = \dot{\gamma}_0 \exp\left(-\frac{F_0}{\kappa\theta}\right) \left(\frac{|\tau_c^\alpha - B_c^\alpha|}{\hat{\tau}_{0c}}\right)^{p_c} \text{sgn}(\tau_c^\alpha - B_c^\alpha) \quad (8)$$

where $\dot{\gamma}_0$ denotes the reference shear strain rate, F_0 the activation energy, κ the Boltzmann constant and θ the temperature in Kelvin. $\hat{\tau}_{0c}$ and p_c are the scalar threshold creep stress and the creep exponent, respectively. The evolution of backstress B_c^α is formulated through a saturation value, B_∞ , related to the end of the primary creep stage as follows [51]:

$$\dot{B}_c^\alpha = C_1 \dot{\gamma}_c^\alpha - C_2 |\dot{\gamma}_c^\alpha| B_c^\alpha = h_c (\dot{\gamma}_c^\alpha B_\infty - |\dot{\gamma}_c^\alpha| B_c^\alpha) \quad (9)$$

where, h_c is a material parameter.

Equations (2)-(9) together with the flow rule and the hardening rule associated with dislocation glide lead to a coupled nonlinear equation system, with $\boldsymbol{\tau}$, \mathbf{R}^e , glide resistance S^α , glide backstress B^α and climb backstress B_c^α as unknowns. The same operator split method with a two-level staggering scheme is adopted to solve the nonlinear system. The numerical implementation of the glide and climb based constitutive model is a straightforward generalization of the glide-only model.

The incorporation of dislocation climb mechanism in Eqs. (4)-(9) allows the prediction of primary creep deformations. As observed in experimental creep curves of [24, 56], IN 617 does

not exhibit a clear secondary creep stage. The extension of the present glide-climb model to capture secondary creep is possible and straightforward for evaluation of the creep response of other alloys that exhibit clear secondary creep.

2.2 Cohesive zone modeling (CZM) for creep damage

CZM is a computational approach to track propagation of distinct cracks, where fracture is considered as a gradual process of surface separation that takes place along an extended crack tip (or cohesive zone) resisted by cohesive tractions. Cohesive zone model is advantageous over other fracture mechanics based models, since it does not require the presence of pre-cracks. It can predict the behavior starting from an uncracked configuration, and performs well in the context of nonlinear material behavior. One significant caveat is that, unless coupled with adaptive meshing techniques, the direction of crack propagation is prescribed by the underlying finite element discretization. The CZM approach is therefore particularly powerful in cases, where the path of crack propagation is known a-priori (e.g., cracking along grain boundaries).

The cohesive law is derived from a damage-based cohesive grain boundary potential defined by:

$$\phi = \frac{1}{2\delta_c} (1 - \omega_n) k_n \llbracket u_n \rrbracket^2 + \frac{1}{2\delta_s} (1 - \omega_s) k_t \|\llbracket \mathbf{u}_t \rrbracket\|^2 \quad (10)$$

where, $\llbracket u_n \rrbracket$ and $\llbracket \mathbf{u}_t \rrbracket$ denote the normal and tangential separation vectors, respectively, ω_n the interface damage induced by creep cavitation, ω_s the damage induced by grain boundary sliding, k_n and k_t are the initial stiffness along the normal and tangential directions, respectively, δ_c and δ_s are respectively the critical displacement jump in the normal and tangential directions at the point of complete separation when loaded monotonically:

$$\omega_n = 1 \rightarrow \llbracket u_n \rrbracket = \delta_c; \quad \omega_s = 1 \rightarrow \|\llbracket \mathbf{u}_t \rrbracket\| = \delta_s. \quad (11)$$

In order to idealize progressive creep failure, the cohesive law proposed by Bouvard et al. [6] is employed. The cohesive law is built by considering $\delta_s = \delta_c$, $k_t = \alpha k_n$, and:

$$\omega_c := \omega_n = \omega_s \quad (12)$$

in which, ω_c denotes the creep damage variable. The potential function in Eq. (10) then becomes:

$$\phi = \frac{1}{2\delta_c} (1 - \omega_c) k_n \left(\llbracket u_n \rrbracket^2 + \alpha \|\llbracket \mathbf{u}_t \rrbracket\|^2 \right). \quad (13)$$

The derivatives of the cohesive potential ϕ with respect to the normal and two tangential separations lead to the normal and shear tractions:

$$T_n = \frac{\partial \phi}{\partial \llbracket u_n \rrbracket} = k_n (1 - \omega_c) \frac{\llbracket u_n \rrbracket}{\delta_c} \quad (14)$$

$$\mathbf{T}_t = \frac{\partial \phi}{\partial \llbracket \mathbf{u}_t \rrbracket} = \alpha k_n (1 - \omega_c) \frac{\llbracket \mathbf{u}_t \rrbracket}{\delta_c}. \quad (15)$$

When subjected to compression, the normal traction is described as:

$$T_n = k_c \frac{\llbracket u_n \rrbracket}{\delta_c} \quad (16)$$

where, k_c is the penalty parameter. Equation (16) ensures that the impenetrability across the cohesive interface is satisfied under compressive loading condition through the penalty method. The magnitude of the penalty parameter is chosen as large as possible to limit interpenetration. Setting this parameter to extremely large values is known to result in numerical convergence difficulties.

Creep damage evolution is idealized using a power law in the following form [6]:

$$\dot{\omega}_c = \frac{1}{(1 - \omega_c)^p} \left\langle \frac{\|\mathbf{T}\| - T_c}{C} \right\rangle^r \quad (17)$$

where T_c , C , p and r are model parameters defining the evolution of the creep damage. T_c denotes a threshold traction, above which creep damage accumulates. The norm of traction vector is defined by:

$$\|\mathbf{T}\| := \sqrt{\langle T_n \rangle^2 + \frac{1}{\alpha} \|\mathbf{T}_t\|^2} \quad (18)$$

where $\langle \cdot \rangle = (|\cdot| + (\cdot)/2)$ denotes the Macaulay brackets, which eliminates the compressive grain boundary tractions from contributing to creep damage evolution.

The CZM model has been numerically implemented via a user defined element (UEL) subroutine in the commercial software Abaqus. At each increment of the nonlinear finite element analysis, the UEL is called at each cohesive zone element to solve the separation-traction equation, perform interface element level integration, and update the incremental local force vector and stiffness matrix. In order to evaluate the cohesive law and determine the creep damage state within the cohesive element, the creep damage variable ω_c of all Gauss points belonging to each cohesive zone element is solved at each time increment through a Newton-Raphson method using a creep damage residual function obtained from the creep damage evolution in Eq. (17). At each time increment, the nodal displacement fields in the global coordinate system and the cohesive zone model parameters (k_n , α , T_c , δ_c , C , p and r) are considered as inputs while the local force vector and the stiffness matrix of each cohesive element are computed and passed back for the finite element assembly and solver operations. The detailed implementation of CZ elements are provided in Ref. [50].

3 Model Preparation

IN 617 is a solid solution strengthened alloy with face center cubic (FCC) lattice structure. While γ' precipitates exist at lower temperature, IN 617 is largely free of γ' phase at tempera-

ture above 750°C [4] and 12 $\{100\}\langle 110\rangle$ slip systems remain active. The microstructure exhibits distinguishable coarse and fine grains and random initial orientation [35] and a bimodal grain size distribution. This section briefly reviews the microstructure generation and meshing process, based on which, the insertion of cohesive zone elements along the grain boundaries is described.

3.1 Microstructure generation

A microstructure reconstruction and meshing work flow has been developed to obtain representative volume discretization for microstructure analysis. The work flow consists of (1) Generation of the microstructure morphology based on experimental data; (2) Volume meshing; and (3) Insertion of cohesive elements between grain pairs.

Microstructure generation is performed using the software DREAM.3D [15]. Experimental EBSD measurements (Fig. 2(a)) are used to extract the microstructure statistical and morphological information (e.g., grain size distributions in Fig. 2(b) and (c)) and construct statistically equivalent microstructures (Fig. 2(d)), based on which surface mesh of individual grains are obtained. The surface mesh of each grain is essentially a collection of triangular facets that enclose the domain of that grain and belongs to either an external boundary of the microstructure, or to the internal grain boundaries. The parallel polycrystal mesher (PPM) software [10] is used to generate the volume mesh of each individual grain using the surface mesh, which is then stitched together to form the volume mesh of the whole microstructure (Fig. 2(e)). Zero-thickness cohesive zone elements are inserted along the grain boundaries (Fig. 2(f)) using the surface mesh information of each grain following a consistent and automated procedure described below.

In general, a microstructure volume must be chosen large enough to be statistically representative. In contrast, the high computational cost of combined CPFE-CZM simulations necessitates the use of the smallest possible microstructure. In order to choose the representative volume element (RVE), a microstructure convergence study was conducted [61] on a series of increasing size microstructures generated using the bimodal grain size distribution (Fig. 2(b)-(c)) and random orientation distribution from the EBSD measurements (Fig. 2(a)). A 144-grain RVE (Fig. 2(e)) is identified to be appropriate for the current study and shows convergence in terms of both overall stress-strain response as well as the local stress distributions. This 144-grain microstructure with edge length of $320\mu\text{m}$ is discretized by 133,372 linear four-node tetrahedral (C3D4) elements (Fig. 2(e)). The 144-grain microstructure is primarily used for calibration, verification and result analysis. Several additional microstructures generated using the same microstructural statistics have been used to assess variability of the response and discussed as needed.

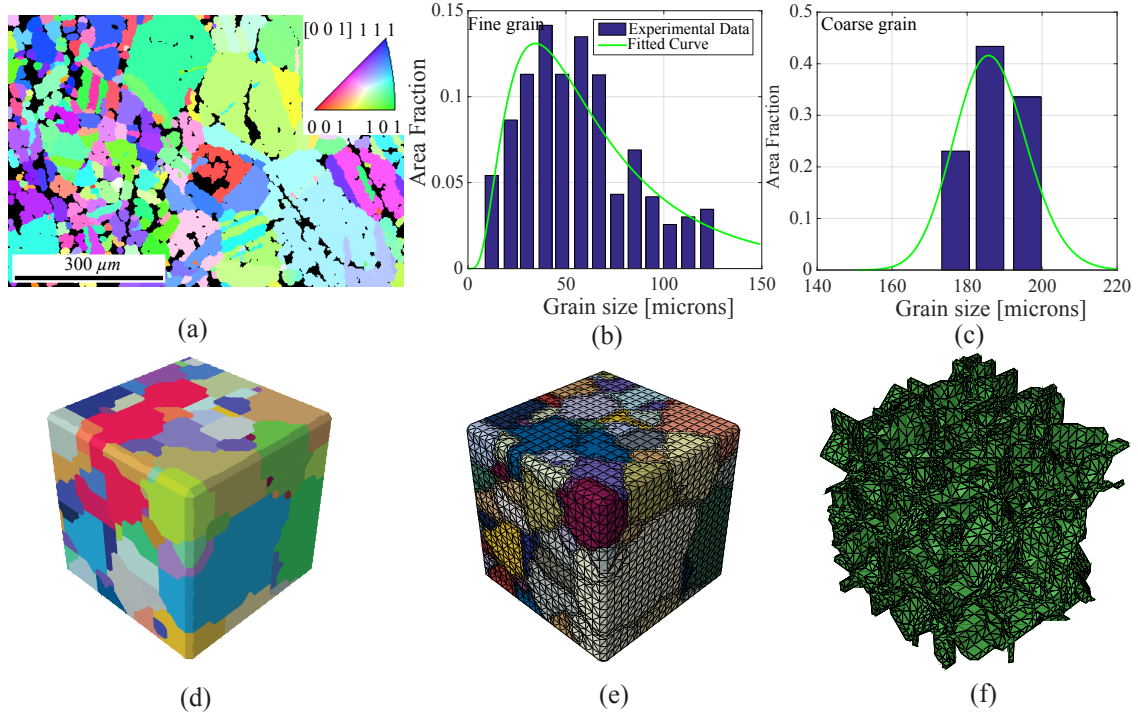


Figure 2: Microstructure reconstruction and meshing: (a) EBSD data; (b)-(c) bimodal grain size distribution; (d) synthetic microstructure reconstruction; (e) volume mesh of the microstructure; (f) zero-thickness cohesive zone elements for grain boundaries.

3.2 Incorporation of cohesive elements

The cohesive elements are embedded into the microstructure mesh using an automated element insertion methodology that defines the element connectivities for arbitrary 3-D microstructures.

The cohesive element incorporation procedure is implemented consistent with the microstructure morphology and surface mesh generation in DREAM.3D and the insertion process only adds cohesive zone element connectivity using grain boundary nodes, leaving the tetrahedral volume mesh of the grains intact. The surface mesh (triangular facets) of each grain either belongs to an external boundary of the representative volume or to the grain boundaries. Nodes on the surface mesh of each grain are assigned a unique node ID. A k-d tree based search process is then conducted to identify the cohesive node pairs (i.e., nodes sharing the same coordinates but belong to two different grains) and subsequently the cohesive face pairs (i.e., two triangle facets formed by three pairs of cohesive node pairs belonging to two different grains) of each grain boundary facet. Each cohesive face pair is used to define a zero-thickness cohesive zone element.

To guarantee the correct calculation of separation and traction, and a positive element Jacobian within the cohesive element, a set of consistent cohesive zone element connectivity construction rules as illustrated in Fig. 3 is defined as follows:

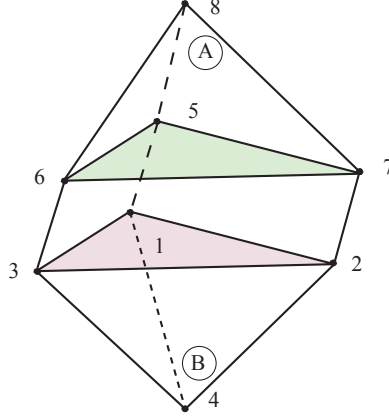


Figure 3: Configuration of the cohesive zone element. Thickness is exaggerated to be nonzero for illustration purpose.

1. One cohesive zone element is inserted between two adjacent bulk elements that belong to two different adjacent grains. As illustrated in Fig. 3, element A and B belong to two different grains with node pairs 6-3, 5-1 and 7-2 being three cohesive node pairs and the blue and green faces being a cohesive face pair. A cohesive zone element is inserted between element A and B using nodes 5, 6, 7, 1, 2 and 3.
2. Element connectivity starts from any node that belongs to one of the two cohesive face pairs, loops over all nodes belongs to that face and then nodes on the other face. We ensure that the ordering of nodes of the face of the first grain (starting from the chosen node), and the opposing face are identical. For instance, starting from node 1 of grain B, either 1-2-3-5-7-6 or 1-3-2-5-6-7 are the two possible connectivities.
3. The normal direction for the starting grain face using the right-hand rule is taken to point to the opposing grain. For instance, the first element connectivity 1-2-3-5-7-6 yields the normal direction of face 1-2-3 pointing away from the second grain while the second element connectivity 1-3-2-5-6-7 has the normal direction of face 1-3-2 pointing to the second grain. The latter is therefore the valid cohesive element connectivity.

The three rules mentioned above provide a consistent cohesive element connectivity definition methodology. Using this procedure, 22,430 cohesive elements are inserted into the above 144-grain RVE to discretize the grain boundaries (Fig. 2(f)), which together with the 133,372 tetrahedral elements form the full discretization of the microstructure.

4 Model Calibration

The parameters of the model associated with the intragranular deformation mechanisms, as well as the intergranular creep damage are calibrated based on experimental data. Model parameters related to the dislocation glide in IN 617 at 950°C have been previously calibrated [61]

and employed as is in this study. Table 1 includes the calibrated parameters that control the dislocation glide. In what follows, the calibration of model parameters related to the dislocation climb and the cohesive grain boundary behavior is discussed. In order to facilitate the calibration process, we first isolate the effects of the dislocation climb parameters by focusing on creep deformation prior to the onset of significant grain boundary damage. The cohesive zone parameters are subsequently calibrated by focusing on creep deformation after grain boundary damage initiation until rupture. Creep tests on IN 617 specimens conducted at Idaho and Argonne National Labs (INL and ANL) have been used to calibrate these parameters [56]. In particular, creep behavior at two applied stress amplitudes of 28.6 and 24 MPa at 950°C are used for calibration.

It is important to note that the number of parameters that describe dislocation climb as well as intergranular damage is high (i.e., 12 parameters). In contrast, only a small number of detailed experiments are available, primarily at the bulk scale. In view of limited calibration data, we rely on: (1) use of previously published data to establish values for some of the parameters and discard them from the calibration set; (2) perform least squares optimization to identify the parameters by minimizing the discrepancy between the experimental and simulated behavior; and (3) ensure that the values of the parameters are within physically meaningful ranges. The third step is necessary, since multiple local minima may result from the optimization process.

4.1 Calibration of dislocation climb parameters

The dislocation climb parameters including the orientation of dislocation climb ψ , the creep exponential parameter p_c , the threshold stress $\hat{\tau}_{0c}$, the saturation stress B_∞ and the primary creep saturation parameter h_c as represented in Eqs. (7), (8) and (9) have been identified. We only focus on the creep-deformation prior to the onset of tertiary creep, where progressive grain boundary damage accumulation using cohesive zone modeling is not included in this calibration step. The calibration process starts with a parametric study to investigate the sensitivity of each parameter in order to identify the ranges for each parameter, where the optimization will be performed. In view of the computational complexity of performing many forward simulations using the CPFEE model within an optimization framework, we first performed the optimizations based on Taylor’s hypothesis [55] to quickly arrive at a set of parameters that provide an acceptable match for the two calibration tests. The identified parameters are further fine-tuned by performing full CPFEE simulations. The creep exponent value is set to be $p_c = 3$ according to the creep strains controlled mainly by climb at high temperatures [36]. It is difficult to determine experimentally the angle ψ , i.e., the average edge/screw ratio since it is related to the measurement of dislocation motion in each slip system during creep deformation process. Therefore, the angle is assumed to be $\pi/4$ that corresponds to a length equal of edge and screw dislocation lines in each face-centered cubic slip system [7, 29]. The remaining parameters are calibrated by minimizing the discrepancy between the experimental

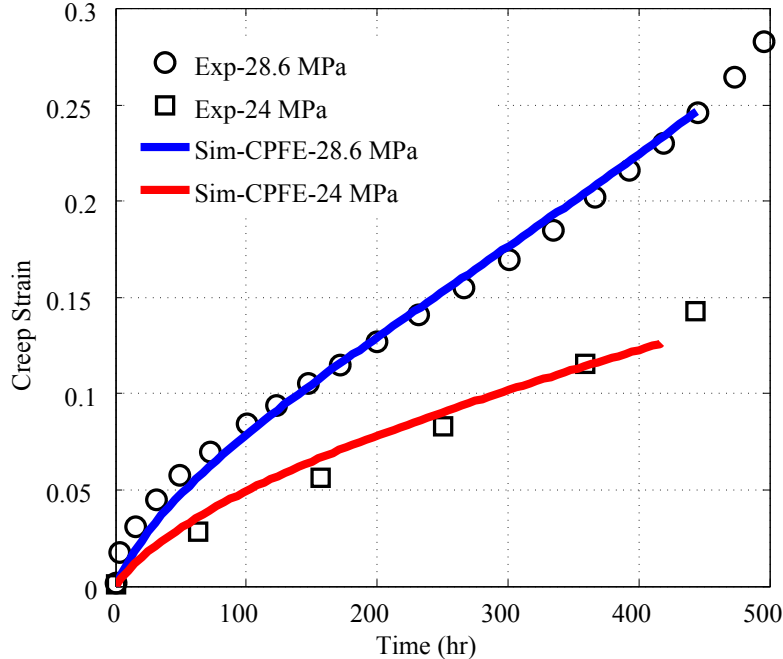


Figure 4: Calibrated results of the creep tests to capture the primary creep at two different stress levels.

and simulated creep curves in the primary stage. The set of parameters that results from the above-mentioned calibration process is shown in Table 1.

The comparisons between simulated creep curves using the calibrated parameters and experimental creep curves for the two different stress levels are shown in Fig. 4. It can be seen that a reasonable match is achieved between the simulated and experimentally observed creep strain evolution as a function of time prior to the onset of grain boundary damage. The yield strength of the material at 950°C is approximately 150 MPa and the applied creep stress amplitudes are substantially lower than yield. We note that in the absence of the climb mechanism, CPFE simulations with only the glide does not show any appreciable creep at stress magnitudes lower than yield. The climb mechanism is therefore primarily responsible for creep strain accumulation at low stress levels. .

4.2 Calibration of cohesive zone model parameters

The combined CPFE-CZM is employed to capture the creep damage behavior at grain boundaries in the tertiary stage. Two of the cohesive zone parameters (k_n and α) correspond to the elastic behavior of the interface. k_n and α are chosen large enough such that no significant separation is observed under normal or shear loading in the absence of damage, while keeping the numerical stability in the simulations. k_n ($= 10^5$ GPa) is identified through a parameter sensitivity analysis. A lower amplitude of k_n results in softening in the elastic region of the stress-strain curves. α is chosen as 0.5 consistent with the prior studies on Nickel alloy mi-

Table 1: Dislocation glide and climb parameters. Glide related parameters are explained in Ref. [61]

C_{11} (GPa)	C_{12} (GPa)	C_{44} (GPa)	$\dot{\gamma}_0$ (s^{-1})	F_0 (J)
170.64	108.39	77.82	1.44×10^{-3}	5.148×10^{-19}
μ_0 (GPa)	μ (GPa)	μ'_0	$\hat{\tau}_0$ (MPa)	f
265.33	77.82	31.13	268.2	0.36
p	q	h_s (MPa)	d_D (MPa)	S_0^α (MPa)
0.181	1.633	397.73	5073.62	143.41
\bar{S}^α (MPa)	h_B (MPa)	h_2 (MPa)	$\dot{\gamma}_{th}$ (s^{-1})	
18.03	104.31	0.015	1.0×10^{-6}	
ψ ($^\circ$)	p_c	$\hat{\tau}_{0c}$ (Pa)	h_c	B_∞ (MPa)
$\pi/4$	3	7,750	32	4.7

crostructures (e.g., [52]). The penalty parameter is taken as $k_c = 10k_n$ [6] in the numerical simulations to constrain against granular interpenetration. Friction is not considered along the grain boundaries following decohesion.

Table 2: Calibrated parameters of the cohesive zone model.

α	k_n (Pa)	δ_c (μm)	r	p	C (Pa)	T_c (Pa)
0.5	10^{14}	450	2.6	3	4.87×10^{10}	8.5×10^6

The remainder of the model parameters for the CZM model is calibrated by minimizing the discrepancy between the experimental and simulated creep curves in the tertiary stage. The intrinsic length parameter δ_c is identified as 450 μm which lies within the range provided by Bouvard et al. [6] and Sun et al. [52]. The threshold traction T_c corresponding to creep strength is assumed to be 8.5 MPa. The exponent p is 3 consistent with that provided in Ref. [52]. The complete set of calibrated CZM parameters is shown in Table 2.

Figure 5 shows the comparison between the numerically simulated and experimental creep curves, where two microstructures (the 144-grain and a 151-grain with identical morphological statistics) are considered. The reasonable match between the experimental and simulated curves indicates that CPFE-CZM model can capture the progressive damage evolution and rupture in the specimens at two stress levels. The experimentally observed rupture times for specimens subjected to 24 MPa and 28.6 MPa are 940 and 566 hours, respectively. The simulated rupture times for the two cases are 1010 and 540 hours, respectively with the 144-grain microstructure. Similarly, the corresponding rupture times predicted by the 151-grain simulation are 1,249 and 690 hours, respectively. Rupture is determined when the intergranular separations are fully developed, and when the simulations lose stability under the applied stress amplitude.

The creep damage evolution in the tertiary stage for the specimen subjected to 28.6 MPa

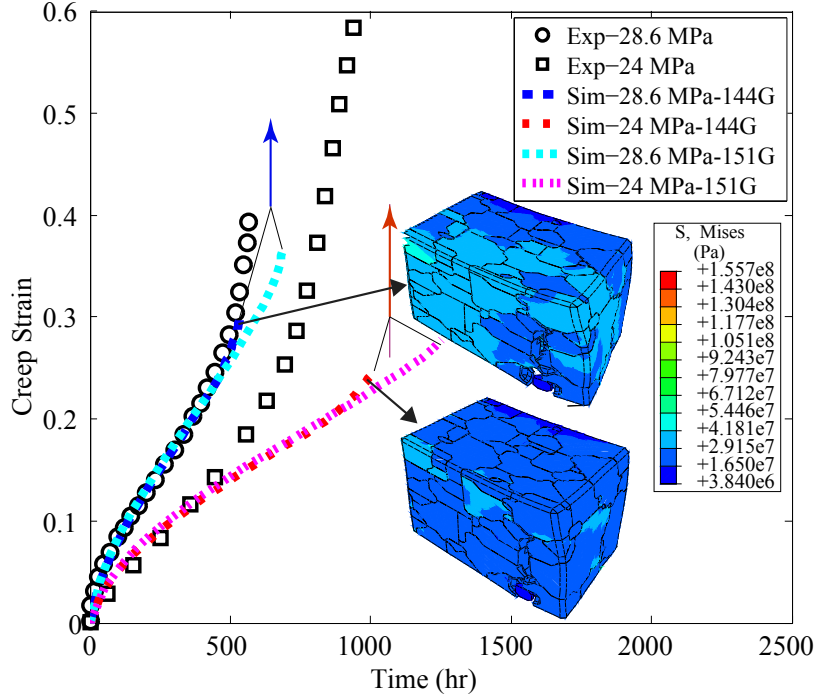


Figure 5: Calibrated results of the creep tests in both primary and tertiary stages for two different stress levels. Dotted lines indicate the presence of GB damage.

has been captured well, whereas the simulated creep strain evolution underpredicts strain rate at the tertiary stage for the 24 MPa case. The simulations also predict a more sudden rupture compared to the experiments.

5 Microstructural Analysis and Validation

5.1 Microstructural analysis

We investigate the state of stress and damage within the microstructure at various creep strain levels to understand the initiation and evolution of grain boundary damage. Figure 6 compares the microstructural stress distributions obtained by CPFE-CZM simulation and glide-climb controlled CPFE simulation (without grain boundary damage) at 12% and 19% creep strains under the applied stress of 28.6 MPa. The stress distributions are very similar between the two models at the strain level of 12%, indicating that there is negligible cavitation and/or sliding at the grain boundaries. This observation is consistent with experimental investigations on the microstructures of crept IN 617 specimens, which did not show appreciable grain boundary cavitation prior to approximately 12% strain levels as discussed in Ref. [32]. At 19% creep strain, significant grain boundary damage is observed in the CPFE-CZM simulation that results in the formation of stress concentrations shown in Fig. 6(d). The stress concentrations in turn accelerate further damage propagation. This behavior is consistent with the observations

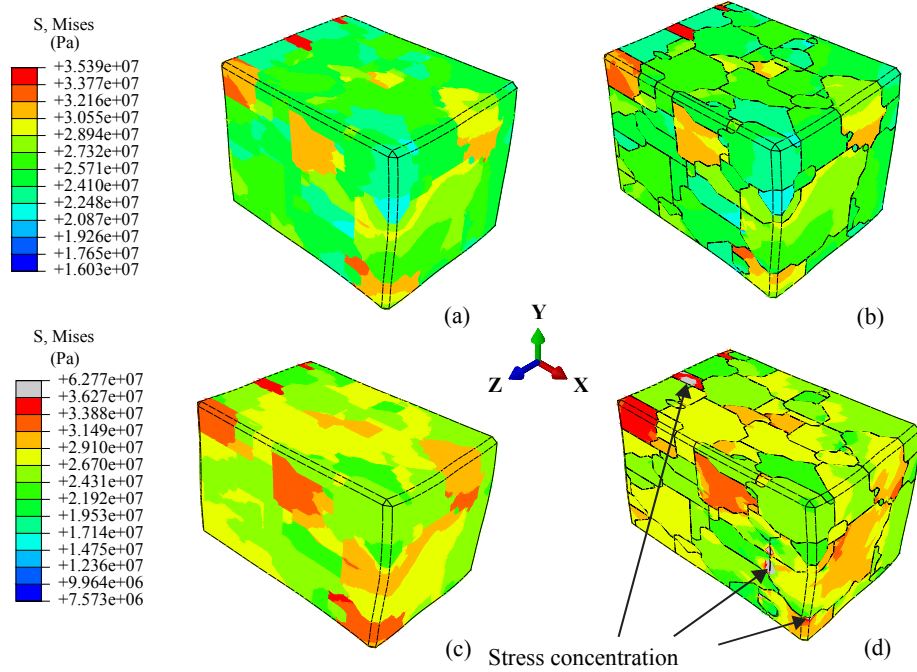


Figure 6: Comparison of stress distribution in the microstructure under 28.6 MPa loading. The CPFE (left) and the CPFE-CZM (right): (a-b) 12% and (c-d) 19% of creep strain at 180 and 347 hours, respectively.

in the literature [47, 58] on the nucleation of grain boundary cavities for metals and superalloys. Figure 7(a)-(b) displays the further growth of grain boundary damage at 25% and 30% creep strains modeled using the CPFE-CZM simulation. The cut views in Fig. 7(c)-(d) show the deformation and grain boundary damage in the interior of the microstructure. The stress levels and the grain boundary separations in the interior of the domain are of similar order of magnitude compared with those observed at the exterior of the microstructure. The figure indicates that the separation initiates at the grain boundary and continues to grow until rupture. The extent and magnitude of separation at the strain level of 30% are very significant, which causes an acceleration of the creep strain rate and immediate rupture in the simulation.

Creep deformation causes significant rotations and grain breakup within the microstructure, particularly near fracture point as shown in Fig. 7. The rotations and grain separations are primarily caused by cavitation, with a relative minor role of sliding (further discussed below). Local rotations and the breakup of grains increase the stress concentrations near the grain boundaries, which further accelerate cavitation as deformation progresses.

Figure 8 shows the deformation of the RVE at the time when the cracks shown in Fig. 7 initiate. All cracks initiate at triple junctions, where three or more grains adjoin each other. Furthermore, cracks initiate at the grain boundaries perpendicular to the loading direction (e.g., between grains 93 and 98, 105 and 42, 136 and 42, 136 and 95, 43 and 10, 43 and 42, 29 and 26, 80 and 122 and grains 5 and 122) and later propagate to the boundaries nearby (e.g.,

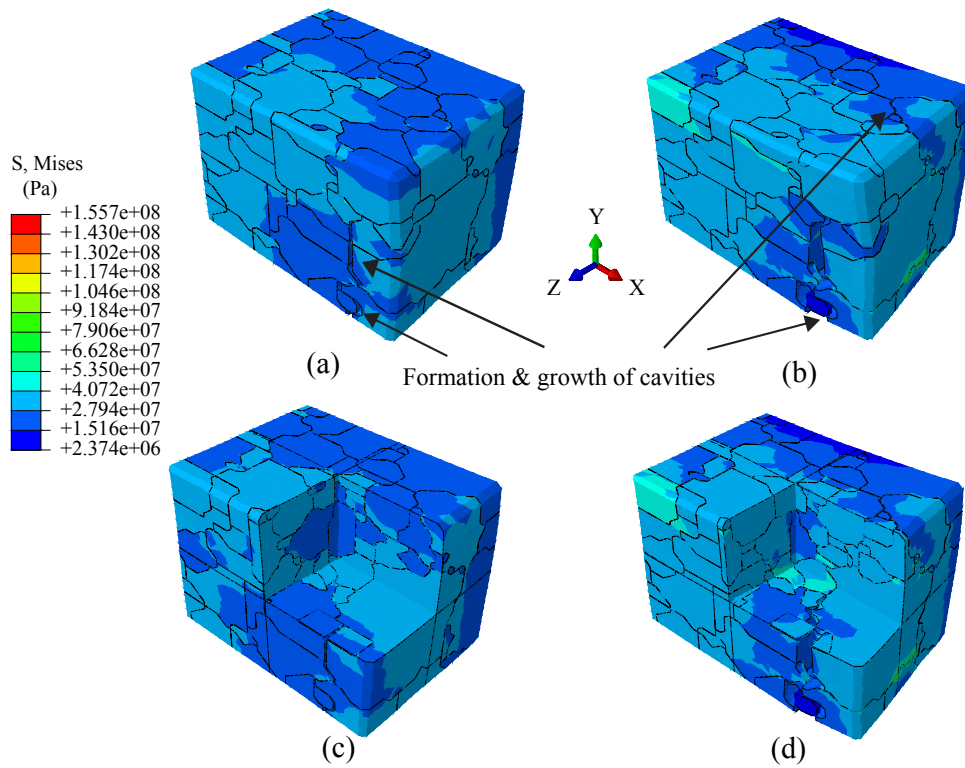


Figure 7: Stress distribution in the microstructure applied by 28.6 MPa loading using the CPFE-CZM: (a) 25% and (b) 30% of creep strain at 472 and 540 hours, respectively; (c) and (d) cut views of (a) and (b).

Table 3: Orientations (Bunge’s convention) and misorientations of grains along the crack initiation sites.

ID of grain A	ID of grain B	Misorientation
93	98	53.26
105	42	28.78
136	42	36.49
136	95	21.09
43	10	41.83
43	42	45.42
29	26	39.49
80	122	47.37
5	122	60.91

between grains 105 and 136 and grains 80 and 5). The misorientations of the grain boundary crack initiation sites in Fig. 8 are calculated in Table 3 using the expression [61]:

$$\theta = \min \left| \cos^{-1} \left\{ \frac{tr(\mathbf{g}_B \mathbf{g}_A^{-1} \mathbf{O}) - 1}{2} \right\} \right| \quad (19)$$

where, \mathbf{g}_A and \mathbf{g}_B are the orientation matrices of adjacent grains A and B , respectively, tr is the trace operator, and \mathbf{O} is the crystal symmetry operator for FCC crystals. The histogram of misorientations of all grain boundaries within the microstructure are shown in Fig. 9. The misorientations on the damage initiation sites are relatively large as shown in Table 3.

In order to illustrate damage nucleation and evolution, the creep damage variable ω_c is plotted along all grain boundaries as shown in Fig. 10 for various states of creep strain. The grain boundary damage initiates at around 12% creep strain state as shown in Fig. 10(a). The growth of damage progresses fairly uniformly across the microstructure (Fig. 10(b)) until approximately 25% creep strain, after which damage localizes to a grain boundary that is perpendicular to the load direction (lower left corner in Fig. 10(c)). Near the point of rupture (Fig. 10(d)) the intergranular crack has propagated significantly. Figure 11 further demonstrates the state of intergranular damage from different viewpoints near the rupture time.

Previous investigations generally relied on the assumption that damage predominantly resides on the grain boundaries oriented perpendicular to the loading direction [9]. Considering the applied stress of 28.6 MPa, Figs. 12-14 illustrate the progressive damage accumulation as a function of creep strain for three different grain boundary orientations. The grain boundary orientation is characterized by the parameter, ϕ , which is the angle between the normal to a cohesive element and the loading direction. In each figure, the evolution of the normalized area fraction of all cohesive elements with angle ϕ are plotted. $\phi = 0^\circ$ indicates that the cohesive elements are perpendicular to the loading direction, whereas, $\phi = 90^\circ$ indicates the cohesive elements are parallel to the loading direction and primarily undergoes sliding. At early stages of the creep process (5%, 12% and 19% of strain), grain boundaries show little damage for all

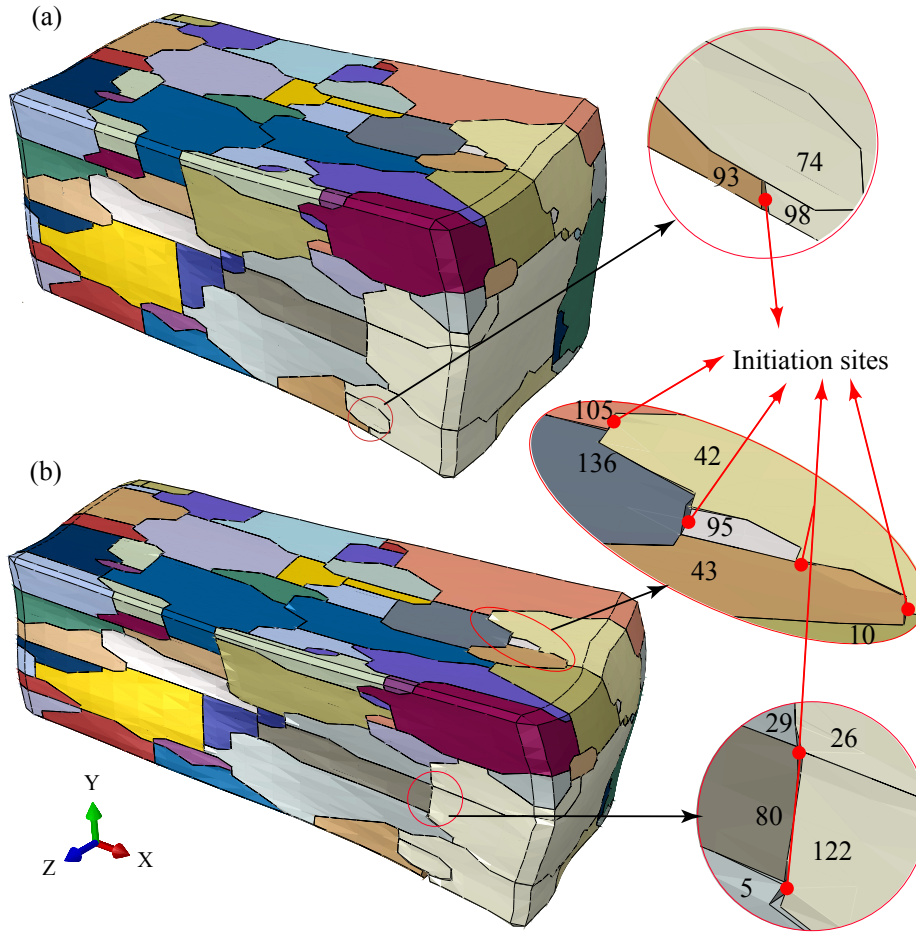


Figure 8: Crack initiation sites at: (a) $t=220$ h and; (b) 355 h. (Different colors indicate different grains with black lines indicating grain boundaries. Numbers indicate grain IDs. Deformation is exaggerated by a factor of 5.)

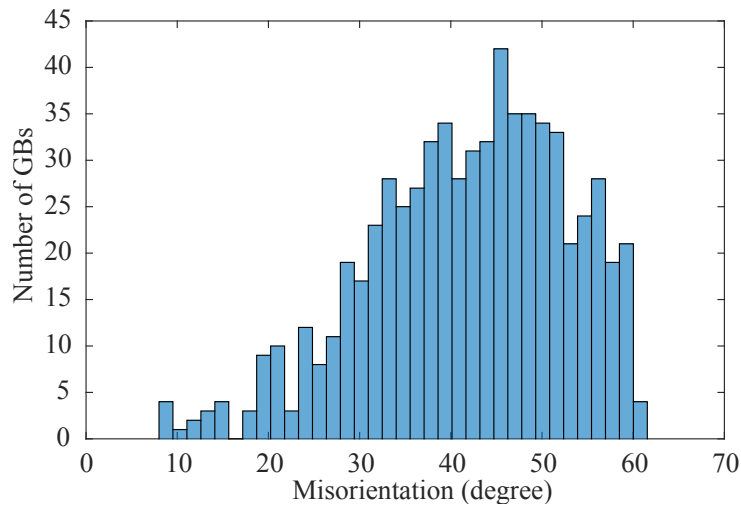


Figure 9: Misorientation of all the grain boundaries in the RVE.

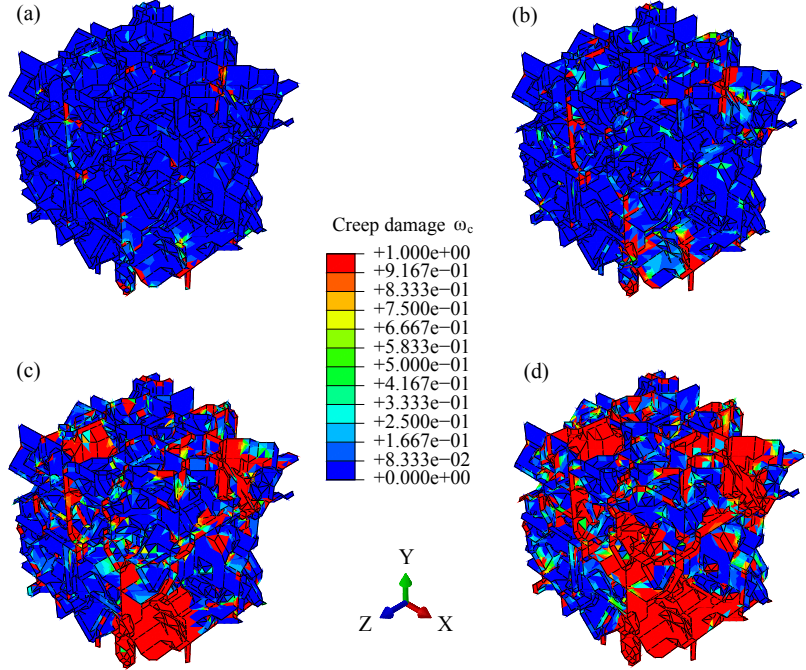


Figure 10: Creep damage evolution represented by cohesive elements in the microstructure under 28.6 MPa loading: (a) 12%, (b) 19%, (c) 25%, and (d) 30% of creep strain at 180, 347, 472 and 540 hours, respectively.

three orientations. As the creep strain increases, more of the grain boundaries incur damage leading to a higher area fraction of grain boundaries with more damage. Two observations are made: First, a large majority of the cohesive zone elements either display no significant damage or complete failure. This implies a sudden damage accumulation process at the local scale. Second, despite the fact that the grain boundaries perpendicular to the loading direction show a much greater extent of damage, those with different orientations and notably those parallel to the loading direction, also display damage. This indicates the possible presence and role of grain boundary sliding in addition to cavity growth.

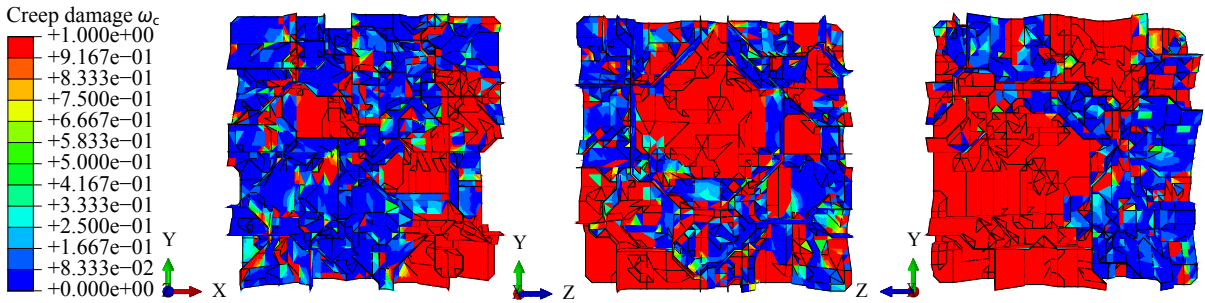


Figure 11: Creep damage contour of the microstructure under 28.6 MPa loading at 30% of creep strain: (a) Front view, (b) Left view, and (c) Right view.

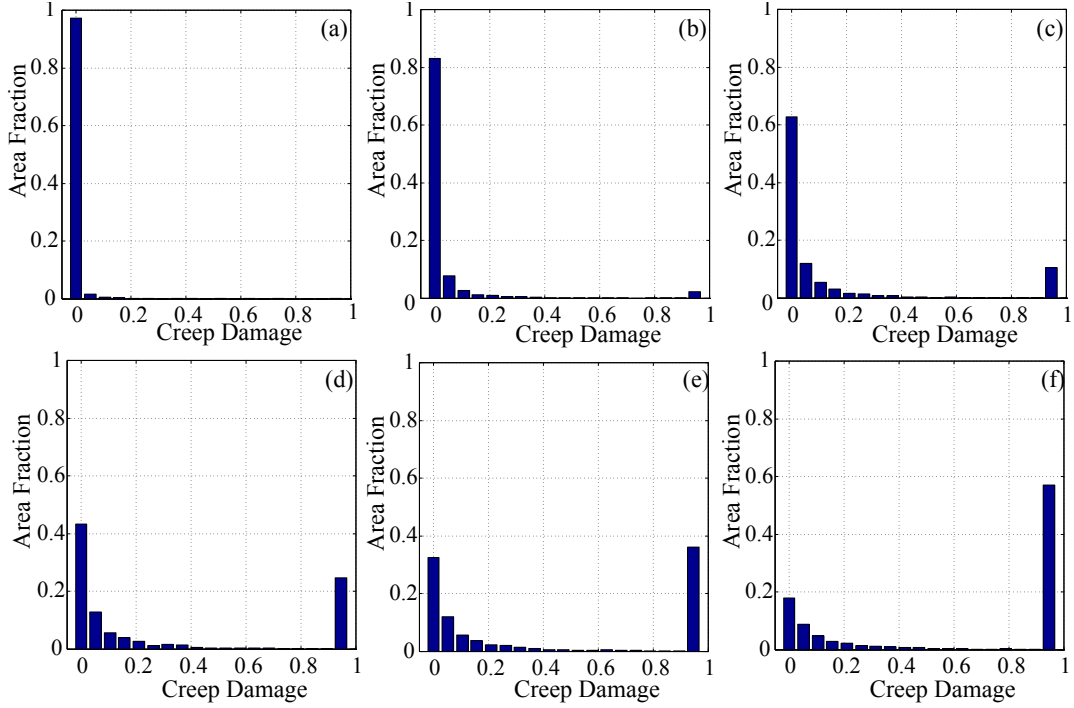


Figure 12: Creep damage distribution of cohesive elements with their normal direction parallel to the creep stress axis ($\phi = 0^\circ$): (a) 8%, (b) 12%, (c) 19%, (d) 22.4%, (e) 25%, and (f) 30% of creep strain.

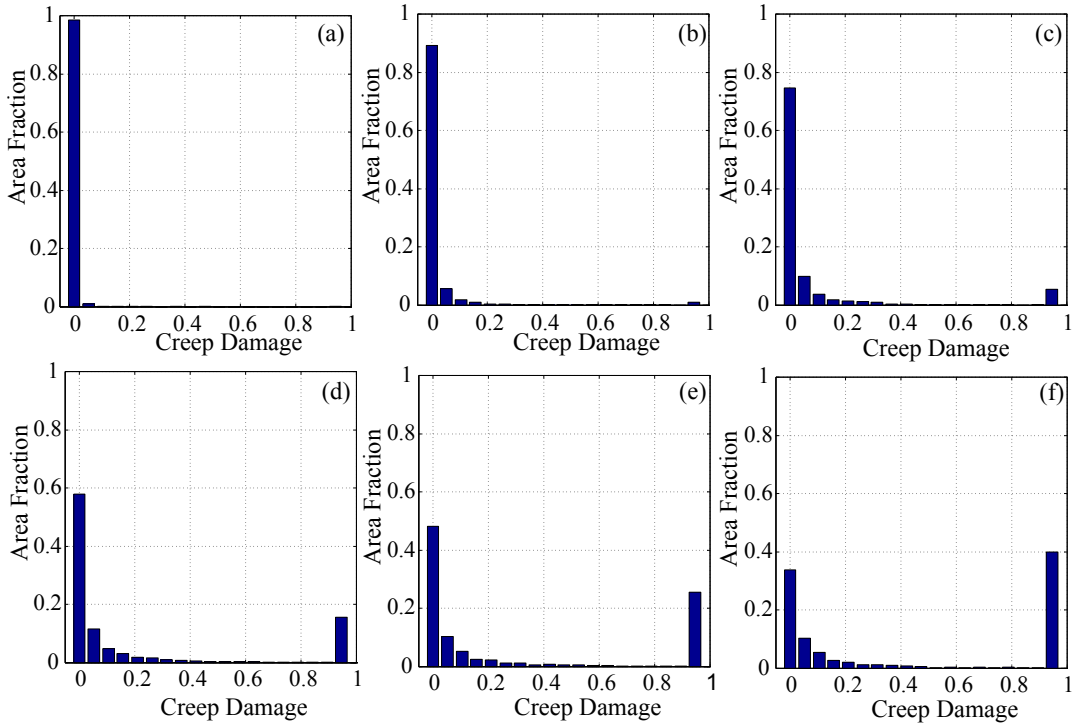


Figure 13: Creep damage distribution of cohesive elements with the angle $\phi = 45^\circ$ between their normal direction and the creep stress axis: (a) 8%, (b) 12%, (c) 19%, (d) 22.4%, (e) 25%, and (f) 30% of creep strain.

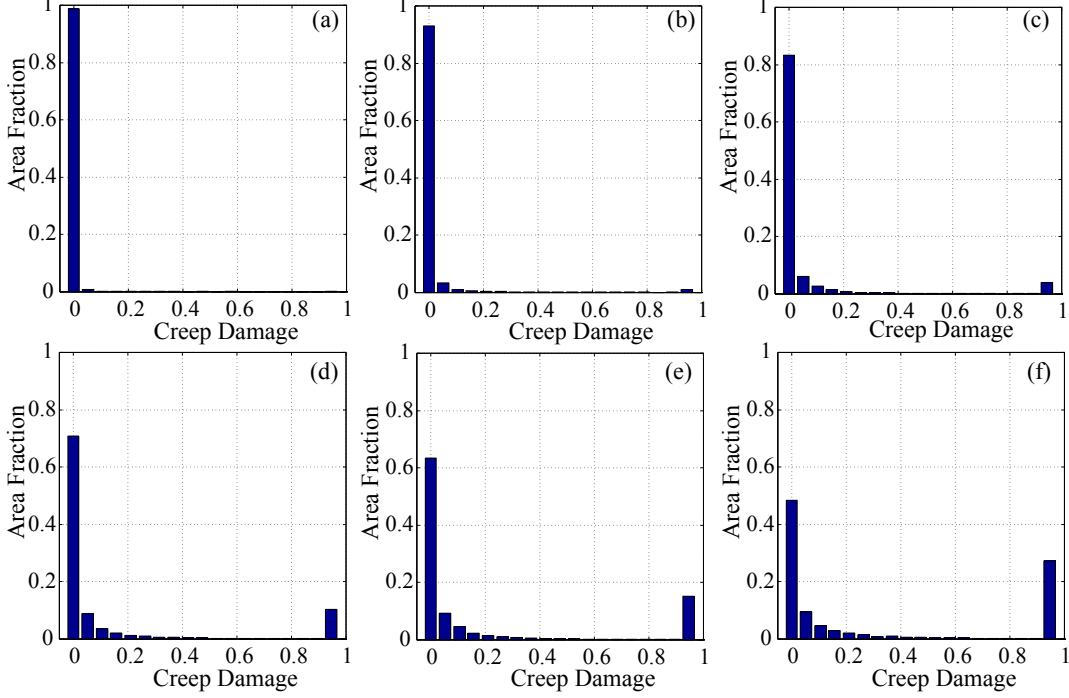


Figure 14: Creep damage distribution of cohesive elements with their normal direction perpendicular to the creep stress axis ($\phi = 90^\circ$): (a) 8%, (b) 12%, (c) 19%, (d) 22.4%, (e) 25%, and (f) 30% of creep strain.

5.2 Validation of creep strength predictions

In order to further validate the predictive capability of the proposed model against available experimental data, creep rupture times are computed for various stress levels at 950°C . Several numerical calculations with different applied stress amplitudes (i.e., at 18.5 MPa, 24 MPa, 28.6 MPa, 35 MPa, 42 MPa, 52 MPa, 62.55 MPa, 68 MPa and 91 MPa) are performed using several microstructures with identical morphological statistics including the 144-grain case. All experimental and simulated data are plotted together as logarithmic stress versus the Larson-Miller parameter (LMP) [28]. The simulation results are plotted as the mean and variance of the predicted values from several microstructure simulations. The basic equation of the LMP [28] is given by

$$\text{LMP} = T[\log(t) + P] \quad (20)$$

where T is the absolute temperature in Kelvin, t is the rupture time in hours, and the constant parameter P is taken as 20. Figure 15 shows the comparison between the experimental and predicted creep rupture data at different stress levels at 950°C . The ANL experiments are the rupture data used in the preceding calibration and microstructure analysis (24 MPa and 28.6 MPa), whereas Kim et al. [26] provides the creep rupture data collected from literature for several different stress levels. The mean and variance of the predicted stress rupture times are in reasonable agreement with the experimental data. The predicted rupture data of high stress

levels (e.g., 68 MPa and 91 MPa) show a slightly shorter life than the experimental rupture life. A slightly longer rupture life is identified for the stress levels lower than 35 MPa. Some of the discrepancies between the predicted and experimental rupture lives are attributed to the variability in the experiments, possibly due to material processing differences in experiments as they were performed independently. We note that the predictive capability of the proposed microstructural model could be further validated with direct microstructural observations, when such data becomes available.

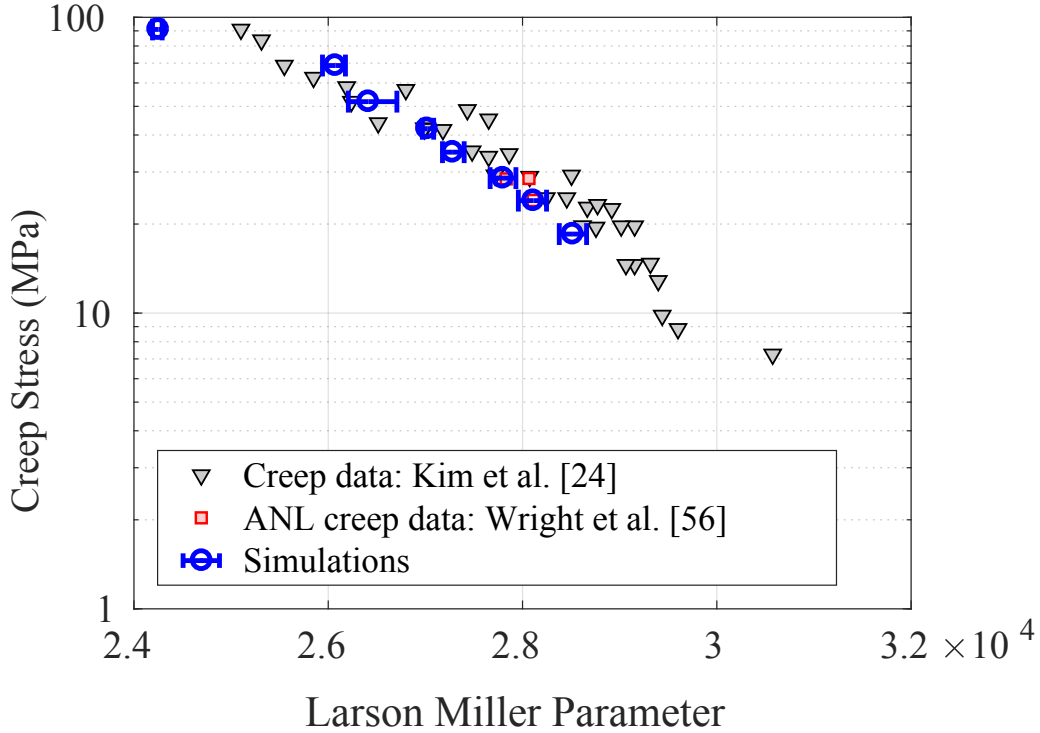


Figure 15: Larson-Miller plot: comparison between simulated results and experimental creep data obtained from ANL creep tests and data from literature.

6 Conclusions

In this manuscript, we presented the formulation, implementation and calibration of a CPFE framework coupled with intergranular progressive damage accumulation modeled using the CZM approach. The proposed model considers the deformation mechanisms of dislocation climb and glide, along with grain boundary damage. The proposed model was employed to investigate the microstructural mechanisms contributing to the degradation of IN 617 under creep loading at 950°C.

The proposed model accurately captures the creep strain evolution and rupture in IN 617, and provides insight into the microscale stress, grain boundary damage distribution and their evolution. The microstructure simulations reveal that (1) Intergranular creep damage

initiates primarily at triple junctions and near high misorientation angle boundaries; (2) The intergranular creep damage accumulation process is sudden at the microscale with intergranular elements displaying either no significant damage or complete failure; (3) Some damage is observed at grain boundaries parallel to the loading direction, indicating a possible presence and role of sliding, in addition to cavity growth. Additionally, a good agreement is obtained between the experimental creep rupture data and corresponding simulations at several applied stress amplitudes. This illustrates the predictive capability of the proposed model.

The proposed model, although calibrated for 950°C only, is expected to be predictive for IN 617 within a range of temperatures between approximately 750-1000°C. Within this temperature range, the microstructure of IN 617 is largely free of γ' precipitates with a relatively stable microstructure, and dislocation climb remains an active deformation mechanism. We note that the elastic properties and the initial slip resistance at the relevant temperature must be identified (or appropriate function form must be incorporated). While this model can be potentially used to model the creep response of other superalloys that exhibit similar deformation mechanisms at high temperature, all or a subset of the model parameters may need to be calibrated specifically for the type of alloy to be studied.

A key interest is the application of the proposed CPFE-CZM model to understand the microstructural failure mechanisms under creep-fatigue loading. Creep-fatigue is a life limiting mechanism in a range of high temperature reactor applications [8, 9]. From the computational perspective, while such detailed CPFE-CZM based microstructure models can accurately capture failure mechanisms, they are computationally very costly. A future focus will be in the development of reduced order algorithms to efficiently simulate the response at a fraction of computational cost [41, 60, 62] and employ such algorithms in the context of multiscale frameworks [39, 40, 59].

7 Acknowledgments

The authors gratefully acknowledge the research funding from the US Department of Energy, Nuclear Energy University Program (Grant No: 62-0476822). We acknowledge the technical cooperation with Prof. Yongming Liu at Arizona State University for providing experimental EBSD data for IN 617, and Dr. Richard Wright at Idaho National Laboratory for providing experimental creep data. The authors would also like to acknowledge Dr. Cerrone from Cornell University for sharing his PPM software for microstructure volume mesh generation as well as helpful discussion on cohesive zone element insertion implementation.

Bibliography

- [1] T. Allen, J. Busby, M. Meyer, and D. Petti. Materials challenges for nuclear systems. *Mater. Today*, 13(12):14–23, 2010.

- [2] A. Argon. Mechanisms and mechanics of fracture in creeping alloys. *Recent Advances in Creep and Fracture of Engineering Materials and Structures*. Pineridge press, Swansea, pages 1–52, 1982.
- [3] G. Barenblatt. The formation of equilibrium cracks during brittle fracture. General ideas and hypotheses. Axially-symmetric cracks. *J. Appl. Math. Mech.*, 23:622–636, 1959.
- [4] J. Benz, T. Lillo, and R. Wright. Aging of alloy 617 at 650 and 750°C. Technical report, Idaho National Laboratory, 2013.
- [5] J. Benz, L. Carroll, J. Wright, R. Wright, and T. Lillo. Threshold stress creep behavior of Alloy 617 at intermediate temperatures. *Metall. Trans. A*, 45:3010–3022, 2014.
- [6] J. Bouvard, J. Chaboche, F. Feyel, and F. Gallerneau. A cohesive zone model for fatigue and creep-fatigue crack growth in single crystal superalloys. *Int. Journal of Fatigue*, 31: 868–879, 2009.
- [7] V.V. Bulatov and W. Cai. *Computer Simulations of Dislocations*. Oxford University Press, Oxford, 2006.
- [8] C. Cabet, L. Carroll, and J. Wright. Low cycle fatigue and creep-fatigue behavior of Alloy 617 at high temperature. *J. Press. Vess. T.*, 135:061401.1–061401.7, 2013.
- [9] L.J. Carroll, C. Cabet, M.C. Carroll, and R.N. Wright. The development of microstructural damage during high temperature creep-fatigue of a Nickel alloy. *Int. J. Fatigue*, 47: 115–125, 2013.
- [10] A. Cerrone, J. Tucker, C. Stein, A. Rollett, and A. Ingrassia. Micromechanical modeling of RENE88DT: From characterization to simulation. In *Proceedings of the 2012 Joint Conference of the Engineering Mechanics Institute and the 11th ASCE Joint Specialty Conference on Probabilistic Mechanics and Structural Reliability*, 2012.
- [11] Albert Cerrone, Paul Wawrzynek, Aida Nonn, Glaucio H. Paulino, and Anthony Ingrassia. Implementation and verification of the Park-Paulino-Roesler cohesive zone model in 3D. *Eng. Fract. Mech.*, 120:26–42, 2014.
- [12] D. Dugdale. Yielding of steel sheets containing slits. *J. Mech. Phys. Solids*, 8:100–104, 1960.
- [13] M.G.D. Geers, M. Cottura, B. Appolaire, E.P. Busso, S. Forest, and A. Villani. Coupled glide-climb diffusion-enhanced crystal plasticity. *J. Mech. Phys. Solids*, 70:136–153, 2014.
- [14] D. Gonzalez, I. Simonovski, P.J. Withers, and J. Quinta da Fonseca. Modelling the effect of elastic and plastic anisotropies on stresses at grain boundaries. *Int. J. Plast.*, 61:49–63, 2014.

- [15] M. Groeber and M. Jackson. DREAM.3D: A digital representation environment for the analysis of microstructure in 3D. *Integr. Mater. Manuf. Innov.*, 3:5–19, 2014.
- [16] S. Hafez Haghghat, G. Eggeler, and D. Raabe. Effect of climb on dislocation mechanisms and creep rates in γ' -strengthened Ni base superalloy single crystals: A discrete dislocation dynamics study. *Acta Mater.*, 61:3709–3723, 2013.
- [17] C.S. Hartley. A method for linking thermally activated dislocation mechanisms of yielding with continuum plasticity theory. *Philos. Mag.*, 83:3783–3808, 2003.
- [18] R. Hu, C. Prakash, V. Tomar, M. Harr, I. Emre Gunduz, and C. Oskay. Experimentally-validated mesoscale modeling of the coupled mechanical-thermal response of ap-htpb energetic material under dynamic loading. *Int. J. Fract.*, 203:277–298, 2017.
- [19] M. Huang, Z. Lia, and J. Tong. The influence of dislocation climb on the mechanical behavior of polycrystals and grain size effect at elevated temperature. *Int. J. Plast.*, 61:112–127, 2014.
- [20] S. Jimenez and R. Duddu. On the parametric sensitivity of cohesive zone models for high-cycle fatigue delamination of composites. *Int. J. Solids and Struct.*, 82:111–124, 2016.
- [21] M.E. Kassner. *Fundamentals of Creep in Metals and Alloys 3rd Edition*. Butterworth-Heinemann, 2015.
- [22] M.E. Kassner and T.A. Hayes. Creep cavitation in metals. *Int. J. Plast.*, 19:1715–1748, 2003.
- [23] S. Keshavarz and S. Ghosh. A crystal plasticity finite element model for flow stress anomalies in Ni₃Al single crystals. *Philos. Mag.*, 95:2639–2660, 2015.
- [24] W. Kim, S. Yin, G. Lee, Y. Kim, and S. Kim. Creep oxidation behavior and creep strength prediction for Alloy 617. *Int. J. Press. Vessels Pip.*, 87:289–295, 2010.
- [25] W. Kim, J. Park, I.M.W. Ekaputra, M. Kim, and Y. Kim. Analysis of creep behavior of Alloy 617 for use of VHTR system. *Procedia Mater. Sci.*, 3:1285–1290, 2014.
- [26] W.G. Kim, J.Y. Park, I.M.W. Ekaputra, S.J. Kim, M.H. Kim, and Y.W. Kim. Creep deformation and rupture behavior of Alloy 617. *Eng. Fail. Anal.*, 58:441–451, 2015.
- [27] D. Kupka, N. Huber, and E.T. Lilleodden. A combined experimental-numerical approach for elasto-plastic fracture of individual grain boundaries. *J. Mech. Phys. Solids*, 64:455–467, 2014.

- [28] F.R. Larson and J. Miller. A time-temperature relationship for rupture and creep stresses. *Trans. ASME*, 74:765–771, 1952.
- [29] R. Lebensohn, C. Hartley, C. Tomé, and O. Castelnau. Modeling the mechanical response of polycrystals deforming by climb and glide. *Philos. Mag.*, 90:567–583, 2010.
- [30] R. Lebensohn, R. Holt, A. Caro, A. Alankar, and C. Tomé. Recent advances in micromechanics of materials: Improved constitutive description of single crystal viscoplastic deformation by dislocation climb. *C. R. Mécanique*, 340:289–295, 2012.
- [31] T. Lillo and R. Wright. Microstructural characterization of Alloy 617 crept into the tertiary regime. *Proceedings of the ASME 2015 Pressure Vessels and Piping Conference, PVP2015*, 2015.
- [32] T. Lillo, J. Cole, M. Frary, and S. Schlegel. Influence of grain boundary character on creep void formation in Alloy 617. *Metall. Trans. A*, 40:2803–2811, 2009.
- [33] E.B. Marin and P.R. Dawson. On modelling the elasto-viscoplastic response of metals using polycrystal plasticity. *Comput. Methods Appl. Mech. Engrg.*, 165:1–21, 1998.
- [34] S.F. Di Martino, R.G. Faulkner, S.C. Hogg, S. Vujic, and O. Tassa. Characterisation of microstructure and creep properties of Alloy 617 for high-temperature applications. *Mater. Sci. Eng. A*, 619:77–86, 2014.
- [35] K. Mo, G. Lovicu, X. Chen, H.M. Tung, J.B. Hansen, and J.F. Stubbins. Mechanism of plastic deformation of a Ni-based superalloy for VHTR applications. *J. Nucl. Materials*, 441:695–703, 2013.
- [36] F.R.N Nabarro. Steady-state diffusional creep. *Philos. Mag.*, 16:231, 1967.
- [37] P. Onck and E. van der Giessen. Microstructurally-based modelling of intergranular creep fracture using grain elements. *Mech. Mater.*, 26:109–126, 1997.
- [38] P. Onck and E. van der Giessen. Micromechanics of creep fracture: simulation of intergranular crack growth. *Comput. Mater. Sci.*, 13:90–102, 1998.
- [39] C. Oskay. Variational multiscale enrichment for modeling coupled mechano-diffusion problems. *Int. J. Numer. Methods Eng.*, 89(6):686–705, 2012.
- [40] C. Oskay. Variational multiscale enrichment method with mixed boundary conditions for modeling diffusion and deformation problems. *Comput. Methods Appl. Mech. Engrg.*, 264:178–190, 2013.
- [41] C. Oskay and J. Fish. Eigendeformation-based reduced order homogenization for failure analysis of heterogeneous materials. *Comput. Methods Appl. Mech. Engrg.*, 196:1216–1243, 2007.

- [42] F. Roters, P. Eisenlohr, L. Hantcherli, D. Tjahjanto, T. Bieler, and D. Raabe. Overview of constitutive laws, kinematics, homogenization and multiscale methods in crystal plasticity finite-element modeling: Theory, experiments, applications. *Acta Mater.*, 58:1152–1211, 2010.
- [43] F. Roters, P. Eisenlohr, T.R. Bieler, and D. Raabe. *Crystal Plasticity Finite Element Methods*. John Wiley and Sons, New York, 1st edition, 2013.
- [44] A. Roy, M. Hasan, and J. Pal. Deformation of Alloys 617 and 276 at 750 – 950°C. *Mater. Sci. Eng. A*, 520:184–188, 2009.
- [45] S.K. Sharma, G.D. Ko, F.X. Li, and K.J. Kang. Oxidation and creep failure of alloy 617 foils at high temperature. *J. Nucl. Mater.*, 378:144–152, 2008.
- [46] M. Shenoy, J. Zhang, and D. McDowell. Estimating fatigue sensitivity to polycrystalline Ni-base superalloy microstructures using a computational approach. *Fatigue Fract Eng M Journal*, 30:889–904, 2007.
- [47] K. Shiozawa and J. Weertman. Studies of nucleation mechanisms and the role of residual stresses in the grain boundary cavitation of a superalloy. *Acta Metall.*, 31, 1983.
- [48] I. Simonovski and L. Cizelj. Cohesive element approach to grain level modelling of intergranular cracking. *Engng. Fract. Mech.*, 110:364–377, 2013.
- [49] I. Simonovski and L. Cizelj. Cohesive zone modeling of intergranular cracking in polycrystalline aggregates. *Nucl. Eng. Des.*, 283:139–147, 2015.
- [50] D. Spring and G. Paulino. A growing library of three-dimensional cohesive elements for use in ABAQUS. *Engng. Fract. Mech.*, 126:190–216, 2014.
- [51] A. Staroselsky and B. N. Cassenti. Creep, plasticity, and fatigue of single crystal superalloy. *Int. J. Solids Struct*, 48:2060–2075, 2011.
- [52] Y. Sun, K. Maciejewski, and H. Ghonem. A damage-based cohesive zone model of intergranular crack growth in a nickel-based superalloy. *Int. J. Damage Mech.*, 22(6):905–923, 2013.
- [53] R.W. Swindeman and Swindeman M.J. A comparison of creep models for Nickel base alloys for advanced energy systems. *Proceeding of ECCC Creep Conference, 12-14 September 2005, London*, 2005.
- [54] F. Tahir, S. Dahire, and Y. Liu. Image-based creep-fatigue damage mechanism investigation of alloy 617 at 950°C. *Mater. Sci. Eng. A*, 679:391–400, 2017.
- [55] G.I. Taylor. Plastic Strain in Metals. *Journal of the Institute of Metals*, 62:307–324, 1938.

- [56] J. Wright, L. Carroll, and R. Wright. Creep and creep-fatigue of Alloy 617 weldments. *Tech. Rep., Idaho National Laboratory*, 2014.
- [57] H. Yang, M. Huang, and Z. Li. The influence of vacancies diffusion-induced dislocation climb on the creep and plasticity behaviors of Nickel-based single crystal superalloy. *Comp. Mat. Sc.*, 99:348–360, 2015.
- [58] J. Zhang. *High temperature deformation and fracture of materials*. Woodhead Publishing, 2010.
- [59] S. Zhang and C. Oskay. Variational multiscale enrichment method with mixed boundary conditions for elasto-viscoplastic problems. *Comput. Mech.*, 55:771–787, 2015.
- [60] X. Zhang and C. Oskay. Eigenstrain based reduced order homogenization for polycrystalline materials. *Comput. Methods Appl. Mech. Engg.*, 297:408–436, 2015.
- [61] X. Zhang and C. Oskay. Polycrystal plasticity modeling of nickel-based superalloy IN 617 subjected to cyclic loading at high temperature. *Modelling Simul. Mater. Sci. Eng.*, 24:055009, 2016.
- [62] X. Zhang and C. Oskay. Sparse and scalable eigenstrain-based reduced order homogenization models for polycrystal plasticity. *Comput. Methods Appl. Mech. Engrg.*, 2017. In press.